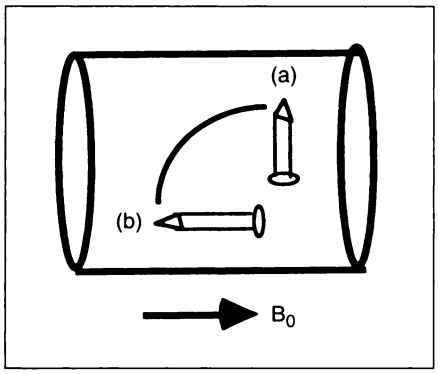

Fig. 1.—Drawing shows orientation of long axis of screw. Note that 90° angle (a) and 0° angle (b) indicate angle of screw in relation to main magnetic field (B_0, *arrow*).

position in the plastic container filled with margarine, and a stainless steel screw with a 6.5-mm thickness, a stainless-steel screw with a 4.5-mm thickness, and a titanium alloy screw with a 6.5-mm thickness were placed in a clockwise rotation. The phantom was positioned at the center of the head coil on a 1.5-T Signa machine (General Electric Medical Systems, Milwaukee, WI). Images were initially obtained in the transverse (short) axis of the screws after the phantom was placed with the long axis of the screws perpendicular to the z-axis of the main magnet (B_0 direction). Next, axial images of the screws were obtained after the phantom was repositioned with the long axis of the screws parallel to the z-axis (Fig. 1). Pulse sequences included spin echo (500/14 [TR/TE]), fast spin echo (500/14; echo train length, 16), and gradient echo (500/14; flip angle, 80°). Common imaging parameters for these three sequences were a 20-cm field of view, a 256 × 256 matrix, one excitation, and a 5-mm slice thickness. Using a fast spin-echo sequence, we evaluated these imaging parameters: matrix size (256 × 128 to 512 × 512), field of view (15–45 cm), slice thickness (3–10 mm), echo time (25 and 100 msec), echo train length (two to 16), and frequency-encoding direction (anteroposterior or superoinferior). Artifact size was measured using the console software and was expressed as the distance between the edges of the middle and lateral lobes of the cloverleaf artifact (Fig. 2). The greatest distance was measured when an artifact was round or oval. Statistical differences in artifact size for the different imaging parameters were evaluated using a simple regression analysis method.

To assess the effect of screw orientation in the magnet, we made a different phantom. A titanium alloy screw (3.5-mm-diameter Titanium Guided Screw) was imbedded at the center of a square plastic container filled with margarine. First, an image was obtained along the coronal plane with the long

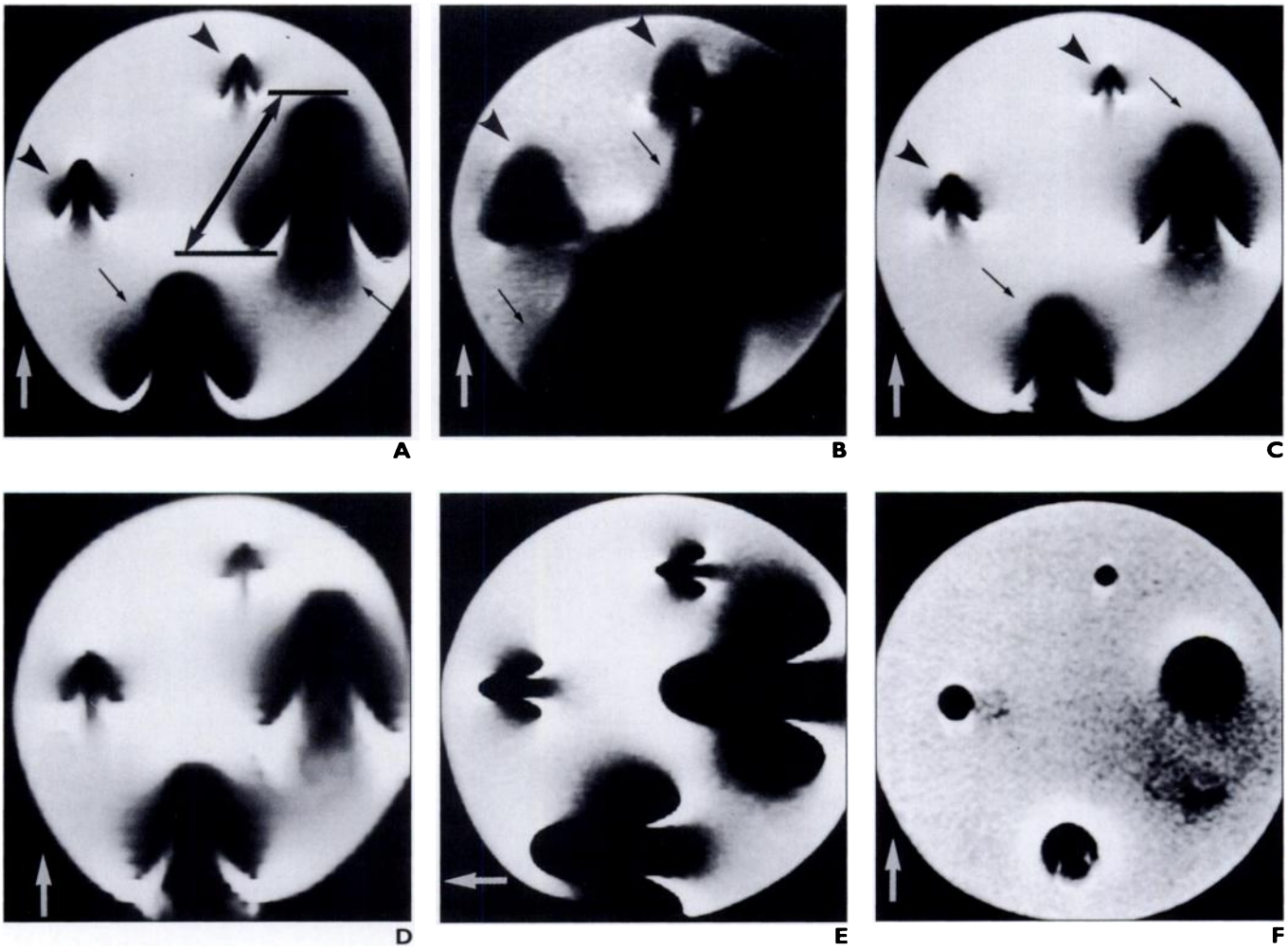

Fig. 2.—Phantom made of plastic, filled with margarine, and filled with both titanium alloy screws (3.5 and 6.5 mm) and stainless steel screws (4.5 and 6.5 mm). Frequency-encoding direction is indicated by white arrows.
A–C, MR images obtained with spin-echo (500/14 [TR/TE]) (**A**), gradient-echo (500/14; flip angle, 80°) (**B**), and fast spin-echo (500/14; echo train length, 16) pulse sequences show that, with phantom placed at 90° angle, screws show cloverleaf-shaped metal-induced artifacts. Note that titanium alloy screws (*arrowheads*) produce smaller artifacts than do stainless steel screws (*thin black arrows*). Also note that least distortion was seen in **C**. Moderate distortion occurred in **B**, and greatest distortion occurred in **A**. Artifact size in this study was determined by measuring distances (shown by *arrow* between lines, **A**).
D, Fast spin-echo MR image obtained with 45-cm field of view shows larger and more blurred artifacts than seen in **C**.
E, Fast spin-echo MR image shows that when frequency direction was swapped, top of cloverleaf-shaped artifacts turned down 90°. However, size of artifacts was unchanged.
F, Fast spin-echo MR image obtained with screws aligned parallel to direction of main magnetic field shows artifacts as round or oval. However, when imaging parameters were changed (not shown), size of artifacts was unchanged.

axis of the screw parallel to the main magnetic field direction; then, consecutive images were obtained at 15° increments along the angle between the long axis of the screw and the main magnetic field direction (Fig. 3). We used a fast spin-echo sequence with the following parameters: 500/20, an echo train length of four, a 15-cm field of view, a 256 × 256 matrix, a 32-kHz receiver bandwidth, a 5-mm slice thickness, and an anteroposterior frequency-encoding axis. The artifact width was measured at the midpoint of the screw.

Patient Imaging

Nineteen patients with metallic implants near the knee were included in our clinical study. Fourteen were men, and five were women; they ranged in age from 20 to 73 years (mean, 41 years). All patients were referred for evaluation of possible internal derangements of the knee, and all had undergone surgical fixation with metallic implants around the knee from a few months to several years previously. The implants were of stainless steel (n = 10) or titanium alloy (n = 9).

All knee MR images were performed on a 1.5-T Signa machine. An extremity coil was used for all patients, and a dual 3-inch (7.6-cm) coil was used when determining the repositioning effect of the knee. In 19 patients, spin-echo sagittal images (2500/20, 70 [TR/first-echo TE, second-echo TE]) were compared with fast spin-echo sagittal images (3500–4000/80–102 [TR range/TE range]; echo train length, eight). The following parameters were used for both pulse sequences: a 14-cm field of view, a 256 × 192–256 matrix, one excitation, and a 3-mm slice thickness with a 1-mm interslice gap. The frequency-encoding axis was set to an anteroposterior direction for all patients. Additional sagittal images were obtained in seven patients after we swapped frequency- and phase-encoding directions. In 15 of the patients, sagittal images of the knee were obtained in flexed and extended positions to compare the effect of repositioning the knee. These MR examinations were undertaken with the patients lying in the decubitus position and the dual 3-inch (7.6-cm) coil applied on the medial and lateral aspects of the knee. In our MR machine, the knees could be flexed from 40° to 100°. We measured the angle between the long axis of the metal and the main magnetic field direction in both the flexed and the extended knee images. The distance was also measured between the metallic implants and the nearest articular surface, using radiographs.

The magnitude of the artifacts and the distortion of the articular structures were compared so as to assess the influence of pulse sequences (the spin-echo and the fast spin-echo sequences), imaging parameters (the frequency-encoding and the phase-encoding directions), and knee positions (the flexed and the extended positions).

Results

Phantom Imaging

The susceptibility artifact had a cloverleaf shape when the long axis of the screw was perpendicular to the main magnetic field direction (Figs. 2A–2E), whereas the artifact was round or oval when the long axis of the screw was parallel to the main magnetic field direction (Fig. 2F). The middle lobes of the cloverleaf artifacts were oriented along the frequency-encoding axis. When we swapped the frequency- and phase-encoding directions, the middle lobes were redirected toward the frequency-encoding axis (Fig. 2E).

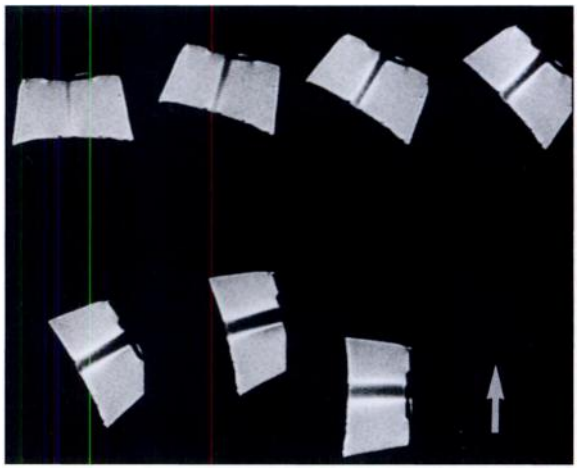

Fig. 3.—Fast spin-echo images of phantom sequentially obtained at 0°, 15°, 30°, and 45° angles (from left in upper row) and at 60°, 75°, and 90° angles (from left in lower row). Size of artifact increases in proportion to increase of angle formed by long axis of screw and direction of main magnetic field (*arrow*). Frequency-encoding direction is identical to direction of main magnetic field.

Throughout our experiments, titanium alloy screws produced smaller artifacts than did stainless steel screws. We also found that the thicker the screws, the bigger the artifacts. Among the three pulse sequences, fast spin echo showed the least geometric distortion, spin echo showed moderate distortion, and gradient echo showed the greatest distortion (Figs. 2A–2C).

When the long axis of the screw was perpendicular to the main magnetic field direction, the magnitude of the artifact was altered by imaging parameters of the fast spin echo such as matrix size, field of view, and slice thickness, which were responsible for determining the voxel size (Table 1). Artifact size correlated positively with voxel size (R^2 = .88, $p < .01$). However, when the long axis of the screw was parallel to the main magnetic field direction, changing the voxel size produced little difference in artifact size. Neither the length of the echo train (two to 16) nor the echo times (25 and 100 msec) influenced artifact size.

The orientation of the screw in the magnet influenced the magnitude of the artifact. The artifact increased in proportion to increases of the angle between the long axis of the screw and the main magnetic field direction (Fig. 3). Artifact size was greatest when the screw was perpendicular to the main magnetic field direction, measuring 2.2 times that obtained when the screw was parallel to the main magnetic field direction.

Patient Imaging

Articular structures were obscured in eight of 10 patients with stainless steel screws because the screws lay less than 30 mm from the articular surface. Loss of structure (cruciate ligament attachment) definition was also found in seven of nine patients with a titanium cannulated screw. This high incidence of obscuration developed because the screw had been fixed near the intercondylar line (–6 to 5 mm). In all patients, the fast spin-echo T2-weighted images showed smaller artifacts than the spin-echo T2-weighted images. The articular structures were more obscure on spin-echo than on fast spin-echo images in eight (42%) of the patients (Fig. 4).

The middle lobe of cloverleaf artifacts was redirected along the frequency-encoding axis in seven patients when we swapped the frequency- and phase-encoding directions. In three of these patients (all of whom had stainless steel screws), articular structures were less obscure when the frequency-encoding axis was in the anteroposterior direction (Fig. 5). In the remaining four patients, with titanium screws, we found no difference in definition of articular structures when the frequency encoding was set to either the anteroposterior or the superoinferior direction.

In five (33%) of the 15 patients whose MR examinations were undertaken with the knee in flexed and extended positions, the articular structures were obscured less at the flexed position (Fig. 6). The angles measured between the long axis of the metallic implants and the main magnetic field direction ranged from 10° to 90° in extension images and from 5° to 90° in flexion images. As had been expected from the experimental results, the knee position and

TABLE 1 Artifact Size of Screw with Respect to Main Magnetic Field and Parameters Determining Voxel with Fast Spin-Echo Imaging

Field of View (cm)	Matrix Size	Slice Thickness (mm)	Voxel (mm^3)	Artifact Size (mm) at the 90° Angle				Artifact Size (mm) at the 0° Angle			
				T1	T2	S1	S2	T1	T2	S1	S2
45	256 × 256	5	15.5	10	14	35	27	4	7	22	20
30	256 × 256	5	6.9	8.5	12	31	26	4	7	19	20
20	256 × 256	10	6.1	7.5	12	30	26	ND	ND	ND	ND
20	256 × 128	5	6.1	7	11	28	24	4	7	22	23
15	256 × 256	10	3.3	ND	ND	ND	ND	4	7	23	20
20[a]	256 × 256	5	3.1	7	12	30	24	ND	ND	ND	ND
20[b]	256 × 256	5	3.1	7	11	28	24	4	7	19	19
20	256 × 256	3	1.8	7	11	28	23	ND	ND	ND	ND
15	256 × 256	5	1.7	6.5	10.5	25	22	4	6.5	19	19
15	256 × 256	3	1.4	ND	ND	ND	ND	4	6.5	19	18
20	512 × 384	5	1.0	ND	ND	ND	ND	4	6.5	19	18
20	512 × 512	5	0.8	ND	ND	ND	ND	4	6.5	17	17

Note.—T1 = 3.5-mm-thick titanium screws, T2 = 6.5-mm-thick titanium screws, S1 = 6.5-mm-thick stainless steel screws, S2 = 4.5-mm-thick stainless steel screws, ND = imaging not done.

[a]This row presents measured data at dual-echo fast spin-echo acquisition (4000/25, 100 [TR/first-echo TE, second-echo TE]). No difference in artifact size was found between the first-echo and the second-echo images (not presented in the table).

[b]This row is a data set with an echo train length of four, and the same results were obtained with echo train lengths of two, eight, and 16 (not presented in the table).

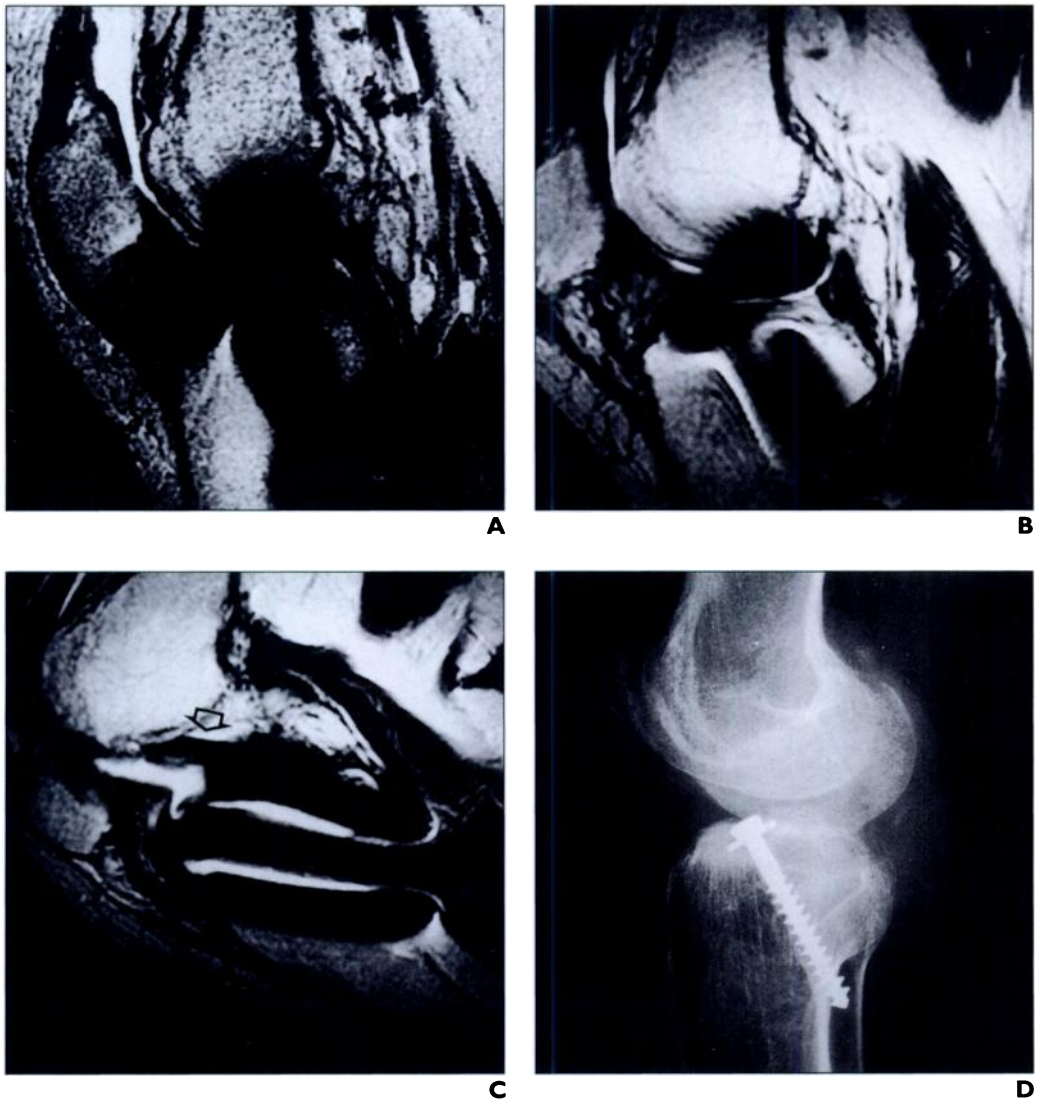

Fig. 4.—25-year-old woman with stainless steel screw in tibia.
A–C, Spin-echo image of knee extension (**A**) and fast spin-echo images of knee extension (**B**) and flexion (**C**) show that meniscus, anterior cruciate ligament, and femoral articular surface are obscured more in **A** than in **B**. In **C**, posterior cruciate ligament (*arrow*, **C**) and distal femur are well visualized. In **A–C**, frequency-encoding direction is anteroposterior.
D, Lateral radiograph shows stainless steel screw in proximal tibia.

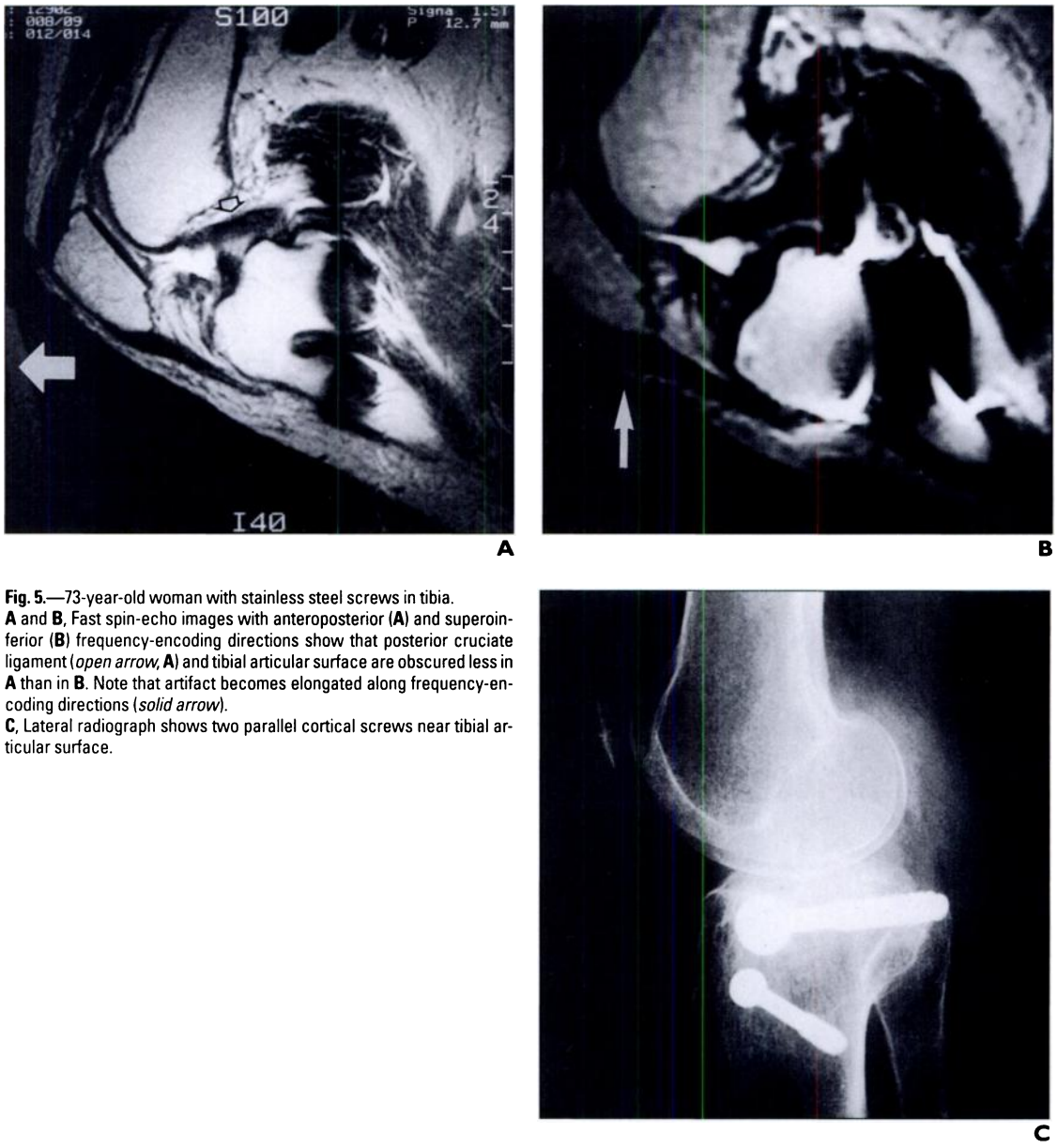

Fig. 5.—73-year-old woman with stainless steel screws in tibia.
A and **B**, Fast spin-echo images with anteroposterior (**A**) and superoinferior (**B**) frequency-encoding directions show that posterior cruciate ligament (*open arrow*, **A**) and tibial articular surface are obscured less in **A** than in **B**. Note that artifact becomes elongated along frequency-encoding directions (*solid arrow*).
C, Lateral radiograph shows two parallel cortical screws near tibial articular surface.

the measured angle affected the degree of articular obscuration: The smaller angle reduced the artifact size. However, in four of these five patients (four with stainless steel implants and one with a titanium alloy implant), articular structures were obscured less on the flexion images, although the measured angles during flexion were equal to or greater than those during extension. This decreased obscuration resulted from exaggeration of the artifacts along the anteroposterior direction (frequency-encoding direction) as opposed to the superoinferior direction. However, no difference was found in articular structures in the remaining 10 patients (three with stainless steel implants and seven with titanium alloy implants) regardless of whether the knee was flexed or extended.

Discussion

Susceptibility artifacts induced by metallic objects have been described in previous MR experimental studies or simulation studies [6–9, 11–14]. In most of the previous experiments, MR examinations to evaluate susceptibility artifacts were performed after placing cylindric metallic objects in the magnet, either parallel or perpendicular to the main magnetic field. Similar to previous reports, our study also showed cloverleaf-shaped artifacts when cylindric screws were perpendicular to the main magnetic field axis, and the artifacts became round or oval when they were parallel to the main magnetic field axis. However, most metallic implants are randomly oriented with respect to the main magnetic field in clinical circumstances. Our study revealed that the magnitude and shape of susceptibility artifacts were mainly affected by the orientation of the metallic implants, and our results supported the belief that obscuration of articular structures could be reduced by repositioning the patients' extremities in clinical imaging studies. We believe that the repositioning method would provide better images in patients with metallic implants than do conventional methods, although our data were not tested by sta-

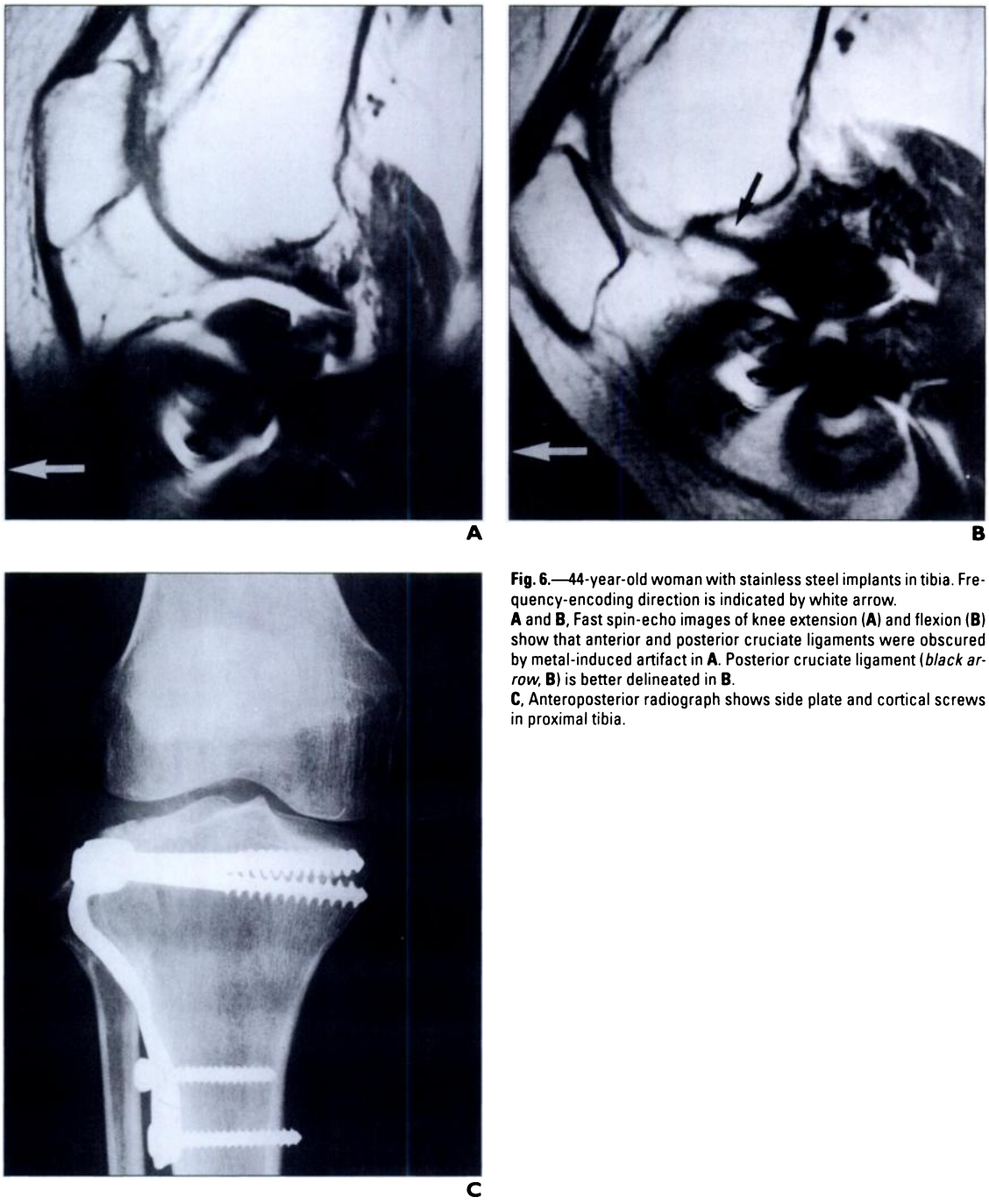

Fig. 6.—44-year-old woman with stainless steel implants in tibia. Frequency-encoding direction is indicated by white arrow.
A and **B**, Fast spin-echo images of knee extension (**A**) and flexion (**B**) show that anterior and posterior cruciate ligaments were obscured by metal-induced artifact in **A**. Posterior cruciate ligament (*black arrow*, **B**) is better delineated in **B**.
C, Anteroposterior radiograph shows side plate and cortical screws in proximal tibia.

tistical analysis because our subjects were few. This method can be used for freely movable regions of the body such as extremities and may be applicable in reducing metal-induced artifacts in any regions of interest if an open magnet is available. However, the complexity of hardware configurations, the unpredictability of hardware orientations, and the lack of availability of radiographs create problems in the optimization of patient positioning and image quality. In many cases, optimization may not be feasible.

Our study also showed that the direction and extent of geometric distortion were governed by the direction of the frequency-encoding axis. Geometric distortions were more exaggerated and elongated along the frequency-encoding axis than along the phase-encoding axis. Thus, if the frequency-encoding direction is chosen, articular structures will be obscured less in clinical imaging studies.

Many previous works have supported the idea that susceptibility artifacts can be affected by gradient strength, pulse sequence, sample bandwidth, voxel size, and echo time [3, 10, 11, 15–24]. Our experiments also revealed that susceptibility artifacts were influenced by pulse sequence, voxel size, and gradient strength. The magnitude of susceptibility artifacts is inversely proportional to gradient strength [10]. Gradient strength, which is determined when a user selects a field of view and matrix size in a certain pulse sequence, is inversely proportional to the size of the voxel. This fact implies that the smaller the voxel, the smaller the artifact. In contrast, echo time in fast spin-echo im-

aging did not play a role in reducing artifact size in our study; the spin dephasing can be rephased by 180° RF pulses [8].

We found susceptibility artifacts to be influenced by the size, shape, and components of the metallic implants, as has been reported previously [19–24]. Titanium alloy produced fewer artifacts than did stainless steel, artifacts were prominent close to the edges of the implants, and geometric distortions depended on the size and shape of the implants.

In summary, susceptibility artifacts can be minimized when the angle between the long axis of the cylindric screws and the axis of the magnetic field is as small as possible. This condition can be met in clinical MR imaging of the knee by positioning patients' extremities adequately. Moreover, articular structures can be obscured less if the frequency-encoding direction is chosen adequately, and susceptibility artifacts can be reduced when imaging voxels are small or when fast spin-echo imaging is used.

References

1. Shellock FG, Morisoli S, Kanal E. MR procedures and biomedical implants, materials, and devices: 1993 updates. *Radiology* **1993**;189:587–599
2. Shellock FG. MR imaging of metallic implants and materials: a complication of the literature. *AJR* **1988**;151:811–814
3. Shellock FG, Crues JV. High-field strength MR imaging and metallic biomedical implants: an ex vivo evaluation of deflection forces. *AJR* **1988**; 151:389–392
4. Simmons A, Tofts PS, Barker GJ, Arridge SR. Sources of intensity nonuniformity in spin echo images at 1.5 T. *Magn Reson Med* **1994**;32:121–128
5. Beuf O, Briguet A, Lissac M, Davis R. Magnetic resonance imaging for the determination of magnetic susceptibility of materials. *J Magn Reson B* **1996**;112:111–118
6. Bakker CJG, Bhagwandien R, Moerland MA, Ramos LM. Simulation of susceptibility artifacts in 2D and 3D Fourier transform spin-echo and gradient-echo magnetic resonance imaging. *Magn Reson Imaging* **1994**;12:767–774
7. Bakker CJG, Moerland MA, Bhagandien R, Beersma R. Analysis of machine-dependent and object-induced geometric distortion in 2DFT MR imaging. *Magn Reson Imaging* **1992**;10:597–608
8. Schenck JF. The role of magnetic susceptibility in magnetic resonance imaging: MRI magnetic compatibility of the first and second kinds. *Med Phys* **1996**;23:815–850
9. Ludeke KM, Roschmann P, Tischler R. Susceptibility artefacts in NMR imaging. *Magn Reson Imaging* **1985**;3:329–343
10. Petersilge CA, Lewin JS, Duerk JL, Yoo JU, Ghanayem AJ. Optimization of parameters for MR evaluation of the spine with titanium pedicle screws. *AJR* **1996**;166:1213–1218
11. Posse S, Aue WP. Susceptibility artifacts in spin-echo and gradient-echo imaging. *J Magn Reson* **1990**;88:473–492
12. Bhagandien R, van Ee R, Beersma R, Bakker CJG, Moerland MA, Lagendijk JJW. Numerical analysis of the magnetic field for arbitrary magnetic susceptibility distributions in 2D. *Magn Reson Imaging* **1992**;10:299–313
13. Bakker CJG, Bhagandien R, Moerland MA, Fuderer M. Susceptibility artifacts in 2DFT spin-echo and gradient-echo imaging: the cylinder model revisited. *Magn Reson Imaging* **1993**;11:539–548
14. Yamada N, Imakita S, Sakuma T, et al. Evaluation of the susceptibility effect on the phase images of a simple gradient echo. *Radiology* **1990**;175:561–565
15. Cho ZH, Ro YM. Reduction of susceptibility artifact in gradient echo imaging. *Magn Reson Med* **1992**;23:193–200
16. Kim JK, Kucharczyk W, Henkelman RM. Cavernous hemangiomas: dipolar susceptibility artifacts at MR imaging. *Radiology* **1993**;187:735–741
17. Tartaglino LM, Flanders AE, Vinitski S, Friedman DP. Metallic artifacts on MR images of the postoperative spine: reduction with fast spin-echo techniques. *Radiology* **1994**;190:565–569
18. Vinitski S, Mitchell DG, Einstein SG, et al. Conventional and fast spin-echo MR imaging: minimizing echo time. *J Magn Reson Imaging* **1993**; 3:501–507
19. Augustiny N, von Schulthess GK, Meier D, Boesiger P. MR imaging of large nonferromagnetic metallic implants. *J Comput Assist Tomogr* **1987**;11:678–683
20. Shellock FG, Mink JH, Curtin S, Friedman MJ. MR imaging and metallic implants for anterior cruciate ligament reconstruction: assessment of ferromagnetism and artifacts. *J Magn Reson Imaging* **1992**;2:225–228
21. Ebraheim NA, Savolaine ER, Zeiss J, Jackson WT. Titanium hip implants for improved magnetic resonance and computed tomography examinations. *Clin Orthop* **1992**;275:194–198
22. Ebraheim NA, Savolaine ER, Stintgen SH, Jackson WT. Magnetic resonance imaging after pedicular screw fixation of the spine. *Clin Orthop* **1992**;279: 133–137
23. Rupp R, Ebraheim NA, Savolaine ER, Jackson WT. Magnetic resonance imaging evaluation of the spine with metal implants. *Spine* **1993**;18: 379–385
24. Lyons CJ, Betz RR, Mesgarzadeh M, Revesz G, Bonakdarpour A, Clancy M. The effect of magnetic resonance imaging on metal spine implants. *Spine* **1989**;14:670–672